ROYAL SOCIETY OF CHEMISTRY

PAPER
Luciana Pereira *et al.*
Potential of magnetic silver-coupled zinc and copper ferrite nanoparticles as visible-light photocatalysts towards the degradation of dyes

PAPER

Potential of magnetic silver-coupled zinc and copper ferrite nanoparticles as visible-light photocatalysts towards the degradation of dyes

Ricardo J. C. Fernandes,[abcd] Beatriz D. Cardoso,[e] Ana Rita Silva,[bc] Luciana Pereira [ID] *[bc] and Paulo J. G. Coutinho [ID] [ad]

Increased environmental concerns about water pollution and scarcity have driven the development of innovative processes and technologies to address these issues. Photocatalysis using nanomaterials is auspicious, with proven efficiency in degrading different pollutants. Ferrite nanoparticles (MFe_2O_4) stand out for their dual functionality, photocatalytic activity and potential superparamagnetic behavior, that make them highly appealing for environmental applications, as they facilitate both pollutant degradation and safe recollection, contributing to nanosafety. This work compared two synthesis methods, sol–gel and solvothermal, for synthesizing mixed zinc and copper ferrites ($Zn_{0.5}Cu_{0.5}Fe_2O_4$). Characterization results revealed a bandgap suitable for visible light absorption and superparamagnetic properties reaching 37 emu g^{-1} of saturation magnetization. However, the photocatalytic efficiency of ferrites was minimal due to the recombination of electron–hole pairs (e^-/h^+). Despite that, the ferrites exhibited a high adsorption capacity for the cationic dye Malachite Green (MG), but photocatalytic degradation was low. To suppress the high e^-/h^+ recombination, a novel, fast method, was used to incorporate silver onto the ferrite surface. This modification significantly improved the activity of the ferrites, especially in the nanoparticles synthesized by sol–gel, achieving 90% removal. In contrast, ferrites synthesized by the solvothermal method, beside exhibiting a strong capacity to adsorb MG (55.99%), proved to be photocatalytically inefficient. This highlights the distinct functional strengths of the two synthesis methods, with sol–gel favoring photocatalytic activity and solvothermal favoring adsorption. Relevant parameters, including the amount of silver and nanomaterial concentration, were optimized during the study, resulting in a degradation of 61.89%, at a rate of 0.0381 h^{-1} under visible light. Toxicity tests were also conducted. After irradiation MG samples still exhibited high toxicity towards the bacteria *Vibrio fisheri*, demonstrating that despite color removal, degradation by-products may still be present causing the toxic effect.

Environmental significance

Water pollution from synthetic dyes poses serious ecological and health risks due to their toxicity, persistence, and resistance to conventional treatment. Addressing this challenge requires efficient, reusable, and sunlight-responsive materials. This study presents magnetic $Zn_{0.5}Cu_{0.5}Fe_2O_4$ nanoparticles doped with silver, synthesized *via* a rapid, low-energy process, as visible-light active photocatalysts. The silver-enhanced sol–gel-derived nanomaterials show strong photocatalytic and adsorption capacities, enabling dye removal even in low-light or dark conditions. Their superparamagnetic behavior ensures easy recovery and reuse, minimizing secondary contamination. These findings support the design of safe, effective, and scalable photocatalysts for the treatment of dye-laden effluents, particularly in the final stages of wastewater treatment, aligning with circular economy principles and advancing sustainable water management strategies.

[a] Physics Centre of Minho and Porto Universities (CF-UM-UP), University of Minho, Campus de Gualtar, 4710-057 Braga, Portugal

[b] CEB-Centre of Biological Engineering, University of Minho, Campus de Gualtar, 4710-057 Braga, Portugal. E-mail: lucianapereira@ceb.uminho.pt

[c] LABBELS-Associate Laboratory, Braga/Guimarães, Portugal

[d] LaPMET-Associate Laboratory, 4169-007 Porto, Portugal

[e] Mechanical Engineering and Resource Sustainability Center (MEtRICs), Mechanical Engineering Department, University of Minho, Campus de Azurém, 4800-058 Guimarães, Portugal

1. Introduction

Pollution of the water resources is currently one of the foremost pressing environmental concerns. According to the United Nations Organization, available clean water resources are increasingly dwindling, exacerbated by population growth and the ongoing stress of climate change.[1,2] In addition, the overall quality of existing water reserves is deteriorating at an alarming

rate. Compounding the issue, a wide array of pollutants continuously enter water bodies due to intensive anthropogenic activity, inadequate waste management, and ineffective treatment systems.[3–6] Dyes, widely applied in the textile industry for coloring and printing fabrics, are responsible for about 20% of the wastewater production worldwide.[7] Dyes harm ecosystems, affecting directly and indirectly exposed organisms. By obstructing light penetration, dyes reduce the availability of solar energy to the submerged areas of aquatic systems, severely disrupting aquatic flora.[8] Other organisms can also be exposed to these pollutants, either by direct ingestion or skin contact, or *via* trophic chains, where dyes may be metabolized into more toxic intermediates, for example, aromatic amines.[9] This also presents significant risks to public health, as both some dyes and aromatic amines are known to be carcinogenic.[10] Malachite Green (MG) is a triphenylmethane cationic dye frequently detected in wastewaters, due to its extensive application in industries such as textiles, and in aquaculture as a parasiticide.[11] In aquaculture, it is commonly employed to control fungal infections, protozoan infestations, and various diseases caused by helminths in fish and other aquatic organisms. However, despite its efficacy, the use of MG has raised significant environmental and public health concerns due to its well-documented toxicological effects.[12] Non-biodegradable in nature, MG accumulates in the environment and can infiltrate the food chain, exerting genotoxic, mutagenic, and carcinogenic effects.[13] Upon release into aquatic systems, it undergoes photochemical and biological transformations, primarily *N*-demethylation, hydroxylation, and structural cleavage, leading to the formation of benzophenone-derived by-products, which may be even more toxic and persistent.[12] These concerns have intensified the global demand for efficient and wastewater treatment technologies. Improper disposal or inefficient degradation poses significant ecotoxicological risks to both micro and macro-organisms, potentially leading to severe health and environmental problems.[12,14]

The use of nanomaterials as catalysts to accelerate the photocatalytic degradation of dyes is seen as a promising alternative or a complement to the more traditional wastewater treatment approaches. Photocatalysis, is an eco-friendly and efficient method for degrading persistent pollutants like MG in wastewater, using only a catalyst and a light source, without the need for any chemical addition. It allows the breakdown of chemical bonds of organic compounds through the action of the generated reactive species such as photogenerated holes (h^+), hydroxyl radicals ($OH^•$), as well as superoxide anions (O_2^-).[15] It is energy-efficient, selective towards specific contaminants, and easily scalable. Moreover, photocatalysis can be integrated with other advanced treatment methods, enhancing its effectiveness for environmental remediation. However, the efficiency of the photocatalytic process is highly dependent on the light source due to the different bandgaps of the semiconductor materials. For example, nanomaterials based on titanium dioxide (TiO_2),[16,17] gallium (Ga_2O_3)[18] and indium (In_2O_3)[19,20] exhibit higher efficiency under ultraviolet light. Other nanomaterials, such as ferrites (MFe_2O_4, M = Ca, Mg, Zn, Cu), are active under less energetic wavelengths, including the visible spectrum, due

to their narrow bandgaps.[21] Various ferrite-based materials have also been explored for photocatalytic degradation of dyes. For instance, $Mg_{1-x}Ni_xFe_2O_4$ mixed ferrites have demonstrated efficient degradation of the dye methylene blue, under visible light, exhibiting adsorption of visible light and significant degradation capacity.[22] Similarly, zinc ferrites also demonstrated excellent photocatalytic activity towards the same dye, with a removal efficiency of 96% under visible light.[23] These nanomaterials are also chemically inert and stable, exhibit superparamagnetic behaviour, and are highly efficient at degrading a range of pollutants. Their low-cost and versatility make them particularly suitable for industrial applications.[24–26] Among the studied ferrites, copper ferrites are especially promising due to their capacity to absorb visible light, a property linked to their narrower bandgap of approximately 1.65 eV.[27] The synthesis of mixed ferrites, such as the incorporation of zinc, can enhance the photocatalytic capacity of certain ferrite nanoparticles.[28] Structural rearrangements in nanomaterials lead to increase optical, structural, electric and magnetic properties.[29] Optimizing the magnetic properties is essential, as it allows for the efficient recovery of nanomaterials after the treatment process, preventing possible additional contamination in the final effluent. Furthermore, magnetic nanomaterials can be easily removed from reactors and reused, reducing operational costs and improving the sustainability of the treatment process.

Regarding photocatalytic activity, ferrites such as copper- and zinc-based nanoparticles face certain limitations, particularly the high recombination rate of e^-/h^+ pairs.[30] Coupling these materials with noble metals, such as silver is an excellent strategy to improve the charge separation efficiency and reducing recombination, thereby improving the photocatalytic activity.[31,32] Tsvektov *et al.*[33] demonstrated the preponderance of coupling silver nanoparticles in magnesium ferrites for enhancing photocatalytic degradation of MG. However, no similar positive effect was observed in other ferrites, such as zinc and cobalt ferrites, for the degradation of the same dye.[33] Similarly, Palanisamy *et al.*[34] highlighted the critical role of silver in the nanocomposites structure for visible light absorption, which significantly enhanced the photocatalytic degradation of rhodamine B and methylene blue. Recent advances in organic–inorganic composite photocatalysts have demonstrated significant improvements in pollutant degradation efficiency. For example, Zhang *et al.* (2022)[35] prepared a composite photocatalyst, PDSA/BiO$_{2-x}$, by self-assembling perylene diimide sulfonic acid (PDI) onto BiO$_{2-x}$. This material showed a remarkable increase in the degradation rates of various pollutants, especially for cationic dyes such as rhodamine B and methylene blue, achieving 21-fold and 18-fold increases, respectively, compared to the single-phase BiO$_{2-x}$. These findings highlight the potential of tailored composite systems to enhance photocatalytic performance.

In this study, zinc and copper mixed ferrites, specifically $ZnFe_2O_4$, $CuFe_2O_4$ and $Zn_{0.5}Cu_{0.5}Fe_2O_4$, were synthesized by sol–gel (Sol_ZnCu) and solvothermal (SV_ZnCu) methods, with silver subsequently incorporated through a novel reduction methodology at various concentrations. A new and fast

© 2025 The Author(s). Published by the Royal Society of Chemistry

Environ. Sci.: Adv., 2025, **4**, 1412–1426 | 1413

synthesis methodology was employed for the coupling of silver onto $Zn_{0.5}Cu_{0.5}Fe_2O_4$ nanoparticles ($AgZn_{0.5}Cu_{0.5}Fe_2O_4$ nanoparticles), resulting in enhanced photocatalytic performance while preserving key physicochemical properties such as superparamagnetic behavior. The capability of the resulting material to operate efficiently under low energy irradiation, including exclusive visible light, represents also a significant advantage for reducing operational energy costs in practical applications. The potential of these nanomaterials was evaluated *via* small-scale irradiation assays, using MG dye as a model pollutant. The catalytic efficiency of the nanomaterials synthesized by the two different methods, as well as varying amounts of silver addition, were compared. Additionally, parameters of the photocatalytic process, like the photocatalyst concentration, different irradiation time and wavelength (under UV or visible light) were evaluated.

2. Materials and methods

2.1. Chemicals used

All reagents used in this study were of analytical grade and employed without further purification. The following chemicals were purchased from Sigma-Aldrich (St. Louis, MO, USA): iron(III) nitrate nonahydrate (≥98%), iron citrate tribasic monohydrate (18–20% Fe basis), copper(II) acetate nonahydrate (≥98%), zinc(II) chloride dihydrate (≥98%), nitric acid (ACS reagent, 70%) silver nitrate (≥99%), citric acid (99%), 1-octadecene (≥99.0% GC), oleic acid (≥90%), absolute ethanol (for spectroscopy Uvasol®), D-glucose (99.5% GC), sodium hydroxide solution (% in water), dimethyl sulfoxide (DMSO for spectroscopy Uvasol®), malachite green oxalate salt (dye content ≥90%). For *Vibrio fischeri* assays, negative controls were prepared with the bacterial suspension and a solution of 2% NaCl following ISO 11348-1 and ISO 11348-3 for the toxicity assays. Potassium dichromate ($K_2Cr_2O_7$) at 105.8 mg L^{-1} was used as a positive control.

2.2. Nanoparticles synthesis methods

The synthesis of $Zn_{0.5}Cu_{0.5}Fe_2O_4$ nanoparticles was performed using two distinct approaches, sol–gel and solvothermal. Both methods were adapted from previous works.[31,32] In the sol–gel process, all precursors were dispersed in ultra-pure water: 2 mmol of iron(III) nitrate nonahydrate, 0.5 mmol of zinc chloride dehydrate and 0.5 mmol of copper(II) acetate nonahydrate. The solid amounts were then individually dispersed in ultra-pure water and added drop-by-drop, making up a total volume of 20 mL. The solution was placed under constant stirring until it was thoroughly mixed. Then, 630.42 mg of citric acid was added to the solution and kept at room temperature, with 70 μL of nitric acid being added later to the solution drop-by-drop. The temperature was slowly increased until a brownish gel was formed. After gel formation, the temperature was further increased to evaporate all the remaining aqueous content of the gel until a loose powder was obtained. For the solvothermal synthesis, 2 mmol of iron citrate tribasic monohydrate and 3 mmol of oleic acid were weighed and mixed. Then, 0.5 mmol of copper(II) acetate nonahydrate and 0.5 mmol of zinc(II)

chloride dehydrated were added. 15 mL of octadecene was preheated to 120 °C in a double-neck flask and after reaching the desired temperature, the previous weighted reagents were added. The mixture was kept at 120 °C for one hour. Then, it was heated to 200 °C at a rate of 5 °C min^{-1} and held at that temperature for 100 minutes. After that, the solution was further heated to 290 °C with an increase rate of 1 °C min^{-1} and left under reflux conditions for one hour.

$Zn_{0.5}Cu_{0.5}Fe_2O_4$ prepared by the two methods were calcined under the same conditions (400 °C for 30 minutes). After calcination, the nanomaterials were cleaned with a 1 M hydrochloric acid solution, washed with dimethylsulfoxide (DMSO), and then with ethanol for several cycles. The synthesized $Zn_{0.5}Cu_{0.5}Fe_2O_4$ samples were designated as Sol_ZnCu – and SV_ZnCu corresponding to the sol–gel and solvothermal methods, respectively.

2.3. Preparation of Ag-coupled $Zn_{0.5}Cu_{0.5}Fe_2O_4$ nanoparticles

A reduction process, based on the work of Pugazhenthiran *et al.*[36] was adapted and optimized for nanoparticles silver functionalization. Assays were performed with two different Ag deposition methods: S1 and S2. For S1, 15 mg of nanoparticles were dispersed in 1.5 mL of ultra-pure water and then placed under stirring for several minutes until the nanoparticles were well dispersed. The solution was heated to 60 °C. The following solutions were then added, drop-by-drop: 400 μL of a solution containing 50 mg of silver nitrate in ultra-pure water, 200 μL of 1 mol L^{-1} D-glucose, and 90 μL of a NaOH solution at a concentration of 0.1 mol L^{-1}. For S2, to promote higher dispersion stability of nanomaterials in water, the same quantity of nanoparticles was dispersed in 5 mL of ultra-pure water. Different silver amounts (*i.e.*, ferrite to silver weight ratios of 1 : 1, 1 : 2, 1 : 3.5, 1 : 5, or 1 : 10) dispersed in 1 mL of ultrapure water were added drop-by-drop. After that, 500 μL of 1 mol L^{-1} D-glucose in ultra-pure water and 300 μL of 0.1 mol L^{-1} NaOH were added drop-by-drop. The solution changed from a brownish color, characteristic of ferrites, to black due to the silver reduction at the surface of the nanoparticles. To finalize the process, the nanoparticles were washed repeatedly with water and ethanol for several cycles to remove reaction remains and were placed in an oven for 6 hours at 100 °C. The following samples were synthesized: Sol_$AgZn_{0.5}Cu_{0.5}Fe_2O_4$ synthesized by sol–gel and functionalized with silver (S1); SV_$AgZn_{0.5}Cu_{0.5}Fe_2O_4$ synthesized by solvothermal and functionalized with silver (S1); and samples with different amounts of silver, *i.e.*, Sol_AgZnCu (1 : 1); Sol_AgZnCu (1 : 2); Sol_AgZnCu (1 : 3.5); Sol_AgZnCu (1 : 5); Sol_AgZnCu (1 : 10).

2.4. Characterization of the synthesised nanoparticles

The synthesized nanomaterials were thoroughly characterized to evaluate their structural, morphological, optical, and magnetic properties, ensuring their suitability for photocatalytic applications. Absorption spectra were collected in a double-beam Shimadzu UV-vis-NIR spectrophotometer, model UV-3600 Plus (Shimadzu Corporation, Kyoto, Japan).

Using a Tauc plot, defined by eqn (1), it was possible to estimate the photocatalyst bandgap.

$$(\alpha h\nu)^n = A(h\nu - E_g) \tag{1}$$

X-ray diffraction (XRD) measurements were made using a PAN'Alytical X'Pert Pro diffractometer (Malvern Panalytical Ltd, Malvern, UK) in a Bragg–Brentano configuration operating with Cu K$_\alpha$ radiation ($\lambda = 0.154060$ nm), at the Electron Microscopy Unit of the University of Trás-os-Montes and Alto Douro (UTAD), Vila Real, Portugal. The magnetization measurements were evaluated on an MPMMS3 Superconducting Quantum Interference Device (SQUID) magnetometer Quantum Design MPMS5XL (Quantum Design Inc., San Diego, CA, USA) at IFIMUO (University of Porto, Portugal). The zeta(ζ)-potential values were obtained on a DLS equipment Litesizer™ 500 from Anton-Paar (Anton-Paar GmbH, Graz, Austria) equipped with a laser diode of λ 658 nm. TEM images were obtained using JEOL JEM-1011 high-contrast microscope operating with Cu K$_\alpha$ operating at 100 kV (Centro de Apoio Científico-Technolóxico à investigación (CACTI), Vigo, Spain). The samples were placed under ultrasonication treatment and then deposited on copper grids with carbon and Formvar. Image J was used to analyze the obtained images.

2.5. Photocatalytic assessment of the nanoparticles

The photocatalytic experiments were performed in a lab-scale photoreactor, as demonstrated in Fig. 1. The photoreactor has a 100 W xenon lamp, emitting UV-vis light. Two lenses were used, one to collimate and the other to focus the light on a sample, which is placed in an optical bench. The photocatalytic assays were conducted using samples containing MG aqueous solution at a concentration of 10 mg L^{-1} (0.027 × 10^{-3} mol L^{-1}) and 0.36 g L^{-1} of nanoparticles MG is a triphenylmethane cationic dye that presents a dark blue color when dispersed in ultra-pure water (close to neutral conditions).[12] First, all the samples were left under dark conditions for 1 hour for adsorption/desorption equilibrium. Then, UV or visible light was applied for different periods and aliquots were taken over time. All the aliquots were magnetically decanted and then centrifuged at 10 000 rpm for 10 minutes to remove any solid content. A Shimadzu UV-3600 plus UV-vis-NIR Spectrophotometer (Shimadzu Corporation, Kyoto, Japan) was used to assess the color removal. The difference between the initial dye absorption and the remaining value after stabilization in the dark was used to evaluate the adsorption ($F_{adsorption}$) onto nanomaterials. The removal under irradiation was calculated by

the difference between absorbance at initial irradiation time ($t = 0$) and at the end of the assay. For the final removal ($F_{removal}$) assessment, the correspondent removal under irradiation was calculated and added to the initial adsorbed dye. The dye degradation rate was determined by applying a first-order kinetics model (eqn (2)–(4).

$$F_{adsorption}\ (\%) = 100 - \frac{(I_{dye} - C_0) \times 100}{I_{dye}} \tag{2}$$

$$F_{removal}\ (\%) = F_{adsorption} + 100 - \frac{(C_0 - C_t) \times 100}{C_0} \tag{3}$$

$$C_t/C_0 = F_\infty + (1 - F_\infty)e^{-kt} \tag{4}$$

where I_{dye} is the initial absorption of the dye, C_t is the absorption at a certain time (t), C_0 the absorption time = 0, F_∞ is the fraction of MG molecules that are very slowly photodegraded, t is irradiation time and k the rate.

2.6. Toxicity assessment

Toxicity was assessed using the *V. fischeri* standard method to check if a clear correlation exists between the removal of the dye and the possible detoxification potential of the process in the applied conditions. *Vibrio fischeri* is a highly competent organism for toxicity assessment of water samples, compliant with easy and short-term assays.[37] As *V. fischeri* is a highly sensitive marine organism emitting bioluminescent light, it is possible to correlate the toxicity variations with the pollutant and the photocatalytic process.[38] The bioluminescence intensity decreases according to the toxicity of the tested solutions.[39] Analysis of the treated samples was performed using an adaptation of the standard bioassay "Water Quality – Determination of the inhibition effect of water samples on the light emission of *Vibrio fischeri* (Luminescent bacteria test)" method ISO 11348-1 (ref. 40) and ISO 11348-3,[41] for freshly prepared bacteria, using *V. fischeri* strain NRRL-B-11177 from BioFix® Lumi, from Macherey-Nagel (Düren, Germany), as described by Silva *et al.*[42,43]

Before toxicity analysis, samples were centrifuged (10 min at 10 000 rpm), filtered (Whatman SPARTAN syringe filters, regenerated cellulose, 0.2 μm pore size), and the pH set to values between 6 and 9 with HCl or sodium hydroxide. Salinity and oxygen concentration were tuned to 2% NaCl and 3 mg L^{-1}, respectively. Negative control was prepared with a solution of 2% NaCl, while the positive control was a potassium dichromate solution (105.8 mg L^{-1}).[40,41]

Luminescence was recorded in relative light units (RLU Sec^{-1}), in kinetic mode using a microplate reader (Biotek® Cytation3, Fisher Scientific, Korea), and luminescence inhibition percentage was calculated after 30 min of contact, as stated in ref. 40–42.

3. Results and discussion

3.1. Characterization

Fig. 2 shows XRD results of the prepared samples confirming their crystallinity. Using with Profex software,[44] which is based
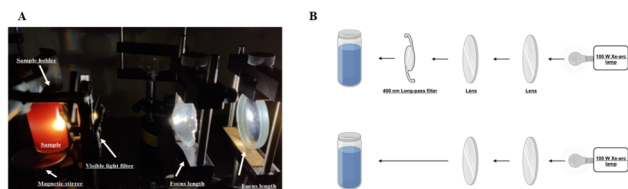

Fig. 1 Photography (A) and schematic representation of the lab-scale photoreactor (B).

© 2025 The Author(s). Published by the Royal Society of Chemistry

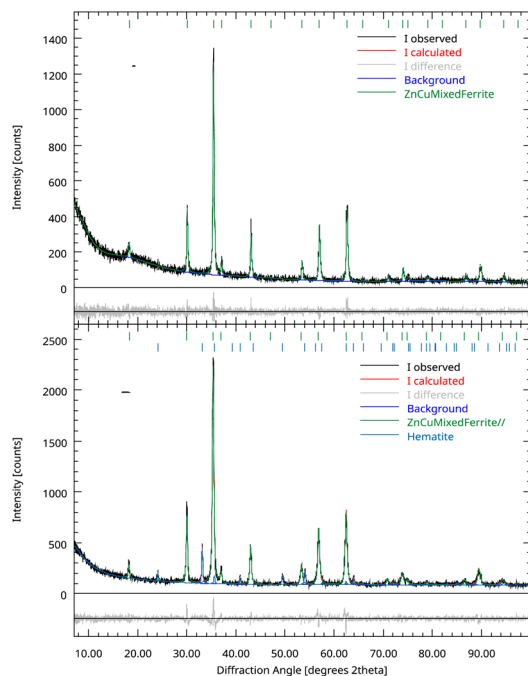*Environ. Sci.: Adv.*, 2025, **4**, 1412–1426 | **1415**

Fig. 2 XRD diffractograms and corresponding Rietveld analysis of obtained Zn/Cu mixed ferrites by solvothermal (A) and sol–gel (B) methods.

on BGMN,[45] Rietveld analysis of the experimental diffractograms were conducted. For that purpose, the zinc ferrite CIF file nr. 2360015 (space group $Fd\bar{3}m$:1) was adapted to a stoichiometric distribution of Cu and Zn cations across both the tetrahedral and octahedral sites over a spinel structure with an arbitrary inversion degree. The sample obtained from solvothermal method exhibited only the mixed ferrite crystalline phase, while the sol–gel method additionally resulted in the formation of a hematite (CIF file nr 9000139; space group $R\bar{3}c$:H) phase, which constitutes 12.0% weight fraction. This new phase is responsible for the additional peaks observed in Fig. 2B. The main results are shown in Table 1.

Reasonable fits were obtained, with R_P values of 7.6 and 8.4 for, respectively, the nanoparticles Sol_ZnCu and SV_ZnCu. The

included lattice constant for of zinc ferrite in the used CIF file is 0.83910 nm. It correspond to $ZnFe_2O_4$ nanoparticles obtained from microwave-assisted growth.[46] Using a solvothermal process the synthesis resulted in nanoparticles with a higher lattice parameter of 0.8420 nm. The lattice parameters of the Zn, Cu mixed ferrites follow similar variations with the preparation method, with the sol–gel route originating a higher lattice value. Also, the similar size of Cu^{2+} and Zn^{2+} (73 pm $vs.$ 74 pm) makes us expect a very small impact on ferrite crystal structure upon substitution of Zn^{2+} with Cu^{2+}. Size estimation of the Zn, Cu mixed ferrite was obtained using the size broadening effect implemented by BGMN and resulted in 37.9 nm and 26.4 nm for respectively the SV_ZnCu and Sol_ZnCu samples. The size of the hematite phase in the latter sample was estimated to be 49 nm.

The absorption spectrum of $Zn_{0.5}Cu_{0.5}Fe_2O_4$ synthesized by sol–gel and solvothermal methods is represented in Fig. 3. Both synthesized nanomaterials show an absorption that steadily increases with energy in measured spectral region. The results demonstrate that silver alters the spectrum, especially in higher wavelengths. The non-appearance of a plasmonic band of silver could be explained by a thick layer of silver, reflecting light, leading to an apparent constant absorption. By applying a Tauc plot, two slightly different bandgaps were estimated. A direct bandgap of 1.97 eV was calculated for sol–gel synthesized nanomaterials, while the solvothermal method determined a direct bandgap of 1.82 eV. Both results fell within the range of possible values reported in the literature.[47] The calculated bandgaps allow efficient visible light absorption.

The nanoparticles' crystal structure, morphology, and size distribution were determined using TEM. The images of sol–gel, solvothermal and silver functionalized nanoparticles elucidate a cubic structure with slightly more rounded nanoparticles in Sol_ZnCu (Fig. 4a–c). The cubic structure seems to be much more well-defined for nanoparticles obtained by solvothermal methodology (Fig. 4d–f). Silver deposition over the nanoparticles is more visible in image g than in image h of Fig. 4, due
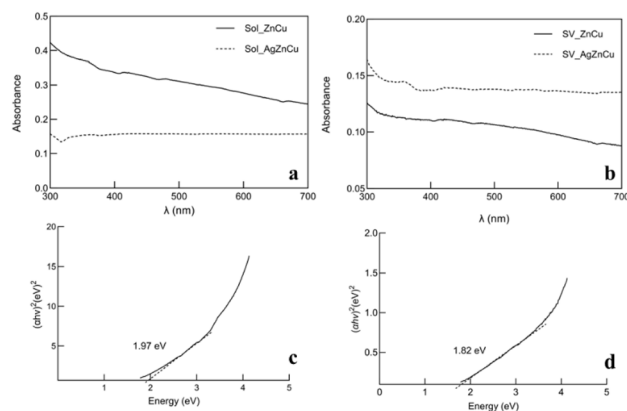
Table 1 XRD diffractograms and corresponding Rietveld analysis of obtained Zn/Cu mixed ferrites by solvothermal (A) and sol–gel (B) methods[a]

Sample	$O_{x,y,z}{}^1$	i	Zn, Cu ferrites	Hematite	R_P	χ^2
			Phase size (nm)			
			Lattice constant (nm)			
Sol_ZnCu	0.3813	0.34	26.4	49 (*)	7.6	1.43
			0.84112			
SV_ZnCu	0.3799	0.51	37.9	—	8.4	1.23
			0.83891			

[a] 1, value of $O_{x,y,z}$ in CIF file 2300615 is 0.2535; i, inversion degree; (*), 3a = 0.50362 and c = 1.3757; R_p, Rietveld refinement pattern fits; χ^2, chi-squared value.

Fig. 3 UV-vis absorption spectra of $Zn_{0.5}Cu_{0.5}Fe_2O_4$ nanomaterials (1 g L^{-1}): (a) synthesized by sol–gel and Ag-doped; (b) solvothermal synthesized $Zn_{0.5}Cu_{0.5}Fe_2O_4$ functionalized with Ag; (c) Tauc plot for $Zn_{0.5}Cu_{0.5}Fe_2O_4$ by sol–gel method; (d) Tauc plot for $Zn_{0.5}Cu_{0.5}Fe_2O_4$ by solvothermal method.
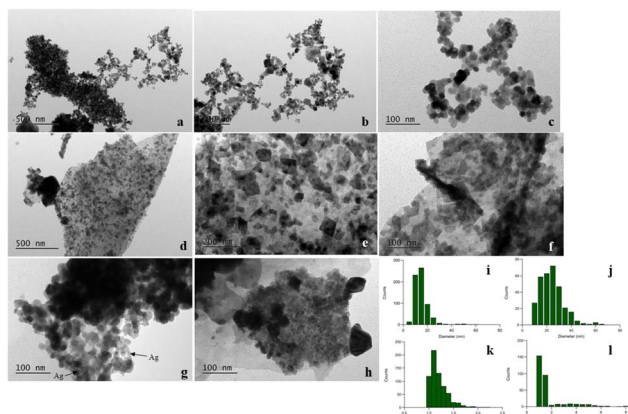
Fig. 4 TEM images of $Zn_{0.5}Cu_{0.5}Fe_2O_2$ nanoparticles synthesized by two different methods (sol–gel and solvothermal), and Ag coupled. (a)–(c) – nanoparticles synthesized by sol–gel method (sol_zncu); (d)–(f) – nanoparticles synthesized by solvothermal method (sv_zncu); (g) and (h) – samples after silver functionalization for sol–gel and solvothermal nanoparticles, respectively; (i) size distribution of sol_-zncu; (j) size distribution of sv_ZnCu; (k) aspect ratio of sol_zncu and (l) aspect ratio of sv_ZnCu. In image (g), the presence of silver particles is marked with an arrow. In image (h), no marker was added, as the silver deposition is less visible due to higher agglomeration of the nanoparticles.

Fig. 5 Magnetic measurements of $Zn_{0.5}Cu_{0.5}Fe_2O_4$ and $Zn_{0.5}Cu_{0.5}$-Fe_2O_4 functionalized with silver. (a) Sol–gel synthesized nanomaterials (Sol_ZnCu and Sol_AgZnCu); (b) solvothermal synthesized nanomaterials (SV_ZnCu and SV_AgZnCu).

to lower agglomeration of nanoparticles. Silver is deposited heterogeneously into the surface of the nanoparticles. This can promote the internal flow of electrons and suppress the undesired recombination usually observed in ferrite nanoparticles.

The two methods of synthesis resulted in distinct morphological features. Sol_ZnCu nanoparticles exhibited a more uniform dispersion pattern, although predominantly anchored onto an apparent large structure. In contrast, a large number of SV_ZnCu nanoparticles tend to form large agglomerates, with noticeable clustering among smaller particles and other components. This tendency to aggregate, may negatively impact their performance. Despite thorough post-synthesis washing, residual structures are still evident, as observed in Fig. 4, where larger aggregates appear to serve as deposition sites for the nanoparticles.

For size estimation, the nanoparticles were manually outlined, considering the diameter of a circle with an equivalent area. A size of (24.6 ± 11.22) nm was calculated for Sol_ZnCu, while SV_ZnCu exhibited a slightly higher size (37.2 ± 10.74) nm. These values are compatible with the ones estimate from XRD measurements. The aspect ratio of the nanoparticles was also analysed using a fit to a rectangle for each individually outlined nanoparticle. The aspect ratio is defined as the ratio of the rectangle's length to its width, serving as an indicator of particle elongation: values close to 1 correspond to approximately spherical particles, whereas higher values indicate more elongated or irregular shapes.

The histograms are also shown in Fig. 4(i)–(l). Compared to previous works, ferrite nanoparticle sizes seem similar despite synthesis method and chemical composition alterations. For instance, $Zn_{0.5}Ca_{0.5}Fe_2O_4$, synthesised using a similar sol–gel methodology, reaches close average particle size values (15 ±
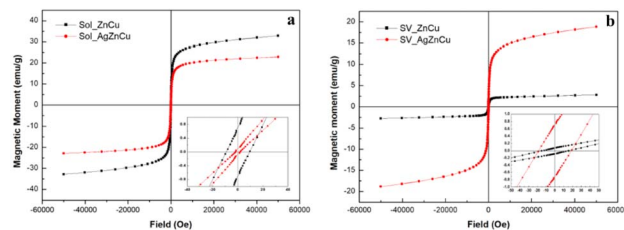
2) nm,[31] while the size was reduced to (10 ± 3 nm) using a coprecipitation method.[48] In another study, solvothermal methodology, resulted in smaller size particles when substituting Cu with Mg (17.4 ± 8.0 nm).[32] The sol–gel method shows limited variation in particle size with precursor variation.

Fig. 5 shows the magnetic measurements for $Zn_{0.5}Cu_{0.5}Fe_2O_4$ and silver functionalized $Zn_{0.5}Cu_{0.5}Fe_2O_4$. Incorporating Cu^{2+} ions into the zinc structure enhanced the magnetic moment, increasing the saturation magnetization of zinc ferrites due to substituting non-magnetic Zn^{2+} with magnetic Cu^{2+}.[49] There is a considerable difference between the Ms values of sol–gel and solvothermal synthesised nanomaterials (Fig. 5 and Table 1). The first one presents a M_s of 32.83 emu g^{-1}, which follows the results of other studies.[50,51] On the other hand, the synthesis by solvothermal method leads to a low M_s of the nanomaterials, 2.80 emu g^{-1}. This may be attributed to the inefficiency of the cleaning process (Fig. 4 TEM), the weight of the non-magnetic mass, and/or even the formation of non-magnetic phases, such as zinc and copper oxides, all of them playing a significant role.

The process of silver functionalization in solvothermal nanomaterials, using the described reduction method, increases the M_s. SV_AgZnCu to 18.76 emu g^{-1}, despite the increased mass addition caused by silver, which, theoretically, should decrease the M_s. Due to the reduction reaction at the surface of the nanomaterials, some of the of the reaction remained by-products, mainly unreacted precursors, residual surfactants, and non-magnetic oxide phases, are washed out during the post-synthesis treatment. Specifically, during the silver functionalization step *via* the described reduction method, Ag^+ ions are reduced to metallic Ag^0 on the nanoparticle surface. This redox reaction not only leads to the deposition of Ag^0 but also promotes the removal of loosely bound or unreacted by-products formed during synthesis, such as residual organics or metal hydroxides, which are non-magnetic in nature. This removal leads to a relative decrease in the non-magnetic mass fraction and consequently leaving the magnetic phase relatively more concentrated. This, in turn, results in an apparent increase in specific magnetization (M_s, emu g^{-1}), as the magnetic response becomes more prominent relative to the reduced overall mass. Silver functionalization under reducing conditions may also promote partial crystallization or reorganization of surface magnetic domains, further

© 2025 The Author(s). Published by the Royal Society of Chemistry

Environ. Sci.: Adv., 2025, **4**, 1412–1426 | **1417**

Table 2 Magnetic measurements and correspondent ζ-zeta potential

Nanomaterial	M_s (emu g^{-1})	M_r (emu g^{-1})	C (Oe)	M_r/M_s	ζ-Potential (eV)
Sol_ZnCu	32.83	0.62	9.44	0.019	-24.97 ± 0.83
SV_ZnCu	2.80	0.10	16.12	0.04	-17.18 ± 0.83
Sol_AgZnCu	23.10	0.08	2.18	0.003	-17.01 ± 0.98
SV_Ag_ZnCu	18.76	0.72	18.64	0.04	-8.02 ± 0.31

contributing to the increased M_s. Sol_ZnCu, contrarily to SV_ZnCu, shows a typical behaviour for silver doping, *i.e.*, a decrease in the M_s attributed to the increase in total mass resulting from silver deposition without significant residue elimination or magnetic phases reordering.

All the nanomaterials presented superparamagnetic behaviour, as evidenced by the ratio between remnant magnetization (M_r) and M_s, which was less than 0.1.[51] The small size of the nanoparticles plays a significant role in promoting this behavior.[52]

The values of ζ-potential obtained for the different synthesized nanomaterials in ultra-pure water (solvent used in the irradiation assays) are presented in Table 2 and in Fig. 6. Zinc and copper ferrites present a typical negative ζ-potential despite variances in ion substitution and synthesis methods.[39,53,54] This was confirmed by the negativity ζ-potential for Sol_ZnCu (-24.97 eV) and SV_ZnCu (-17.18 eV). ζ-Potential indicates affinity for adsorbing cationic molecules such as the MG dye. The reasonably high absolute values of the measured ζ-potential indicate a moderate colloidal stability of the prepared nanoparticles in water. Functionalization with silver increased the ζ-potential to (-17.01 ± 0.98) eV for Sol_AgZnCu and (-8.02 ± 0.31) eV for SV_AgZnCu, although both values remained negative (Fig. 6) so that MG should still be adsorbed.

3.2. Photocatalytic experiments

Conducted small-scale assays allowed for the evaluation of the photocatalytic activity of the synthesized nanomaterials, for the impact of the synthesis method, the effect of varying silver amounts, and the optimal photocatalyst concentration. These assays also explored the influence of different light sources and

Fig. 6 Overall ζ-potential of the synthesized samples in ultrapure water.

prolonged irradiation times, offering critical insights into the photocatalytic process using $Zn_{0.5}Cu_{0.5}Fe_2O_4$, and guiding future optimizations. A preliminary assessment of direct photolysis was also conducted, revealing a degradation of 7.62% over 6 hours under the most powerful light source, UV light (100 W). This result demonstrates the minimal contribution of MG direct photolysis to the overall degradation process. The interplay between initial adsorption and photocatalysis is essential for an optimized degradation of pollutants, as the photogenerated reactive species are allocated on the semiconductor surface.[53] These reactive species interact with and degrade the adsorbed dye molecules. To assess the importance of both processes individually, the solutions containing nanomaterials were placed under dark conditions for one hour to stabilize and analyse the nanomaterials adsorption capacity before irradiation. Table 3 summarizes the results obtained at all the conditions performed.

3.2.1.   Effect of nanomaterial synthesis method. The photocatalytic activity of $Zn_{0.5}Cu_{0.5}Fe_2O_4$ nanomaterials synthesized by sol–gel and solvothermal methods was tested under UV and visible light towards MG as a model pollutant. This study allows for assessing which synthesis method produces nanomaterials with superior photocatalytic activity. The results are presented in Fig. 7. Using Sol_ZnCu, a final MG removal of 43.67% (at a rate of 0.0299 h^{-1}) under UV irradiation, and 19.35% (at 0.0020 h^{-1}) under visible light irradiation, was achieved during 6 h of assay. In contrast, SV_ZnCu showed lower removal values under UV irradiation, 38.59% (at 0.0188 h^{-1}), and higher under visible irradiation, 45.55% (at 0.0029 h^{-1}) (Table 3). Discounting the effect of initial adsorption, it is possible to conclude that photodegradation is very inefficient under visible light irradiation and that Sol_ZnCu nanoparticles have superior performance when using UV light. This might be consistent with the prior characterization results that indicated a cleaner surface (from TEM) that makes the ferrite surface more accessible. Although the zeta potential is more negative for the Sol_ZnCu NPs a lower adsorption is observed. This indicates that organic molecules remain at the surface of SV_ZnCu NPs, as indicated by the TEM images, are good adsorption sites for MG molecules but with low photocatalytic activity as the distance to the ferrite surface is significant. So, the nanomaterials synthesized by the solvothermal method have residues resultant from the synthesis process, which appear to increase the adsorption capacity but inhibit or reduce the photocatalytic efficiency of $Zn_{0.5}Cu_{0.5}Fe_2O_4$.

Upon the incorporation of silver (batch S1), an increase in the dispersion and stability of the nanomaterials was observed. An improvement in the photocatalytic activity was obtained
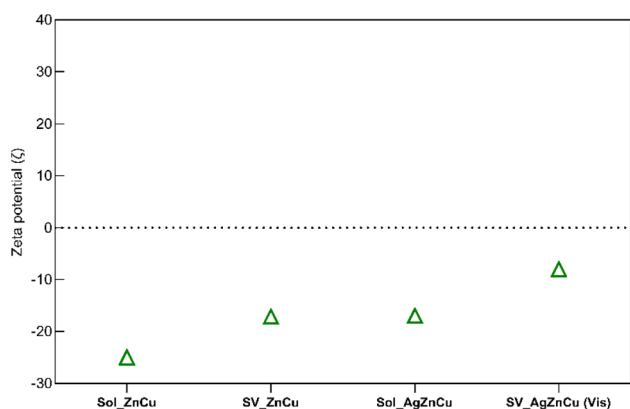
Table 3 Results obtained ofor MG (10 mg L⁻¹) removal by $Zn_{0.5}Cu_{0.5}Fe_2O_4$ nanomaterials at the various conditions, i.e., different nanomaterial concentrations, light source and reaction time

Nanomaterials	Method of silver deposition	Nanomaterial concentration (g L⁻¹)	Light source	Initial adsorption (%)	Removal under irradiation (%)	Irradiation time (h)	Final removal (%)	Final MG concentration (mg L⁻¹)	Rate constant (h⁻¹)
Photolysis		None	UV	—	7.62	6	7.62	9.24	0.0132
Sol_ZnCu	n.a.	0.36	Visible	18.51	1.03	6	19.35	8.07	0.0020
Sol_ZnCu	n.a.	0.36	UV	31.93	17.24	6	43.67	5.63	0.0299
SV_ZnCu	n.a.	0.36	Visible	43.25	4.06	6	45.55	5.44	0.0029
SV_ZnCu	n.a.	0.36	UV	35.51	4.78	6	38.59	6.14	0.0188
Sol_AgZnCu	S1	0.36	Visible	24.99	5.74	6	29.30	7.93	0.0074
Sol_AgZnCu	S1	0.36	UV	36.15	85.37	6	90.66	0.93	0.1589
SV_AgZnCu	S1	0.36	Visible	55.99	0.00	6	55.99	4.40	(*)ᵃ
SV_AgZnCu	S1	0.36	UV	49.12	0.00	6	49.12	5.09	(*)ᵃ
Sol_AgZnCu (1:1)	S2	0.36	Visible	16.26	0.29	6	16.50	8.35	0.0111
Sol_AgZnCu (1:2)	S2	0.36	Visible	31.27	7.78	6	36.61	6.34	0.0186
Sol_AgZnCu (1:3.5)	S2	0.36	Visible	25.98	3.60	6	28.65	7.14	0.0282
Sol_AgZnCu (1:5)	S2	0.36	Visible	19.78	25.69	6	40.39	5.96	0.0665
Sol_AgZnCu (1:10)	S2	0.36	Visible	0	3.52	6	3.52	9.65	0.0068
Sol_AgZnCu (1:5)	S2	0.18	Visible	0	19.55	6	19.55	8.04	0.0334
Sol_AgZnCu (1:5)	S2	0.36	Visible	19.79	25.69	6	40.39	5.96	0.0665
Sol_AgZnCu (1:5)	S2	0.50	Visible	19.49	23.39	6	38.32	6.17	0.0491
Sol_AgZnCu (1:5)	S2	1.00	Visible	24.26	35.40	6	51.08	4.89	0.0982
Sol_AgZnCu (1:5)	S2	0.36	UV	21.47	63.51	12	71.35	2.87	0.1033
Sol_AgZnCu (1:5)	S2	0.36	Visible	18.40	30.20	18	43.05	5.69	0.0218
Sol_AgZnCu (1:5)	S2	0.75	UV	20.18	47.50	12	58.52	4.15	0.0730
Sol_AgZnCu (1:5)	S2	0.75	Visible	24.52	49.50	18	61.89	3.81	0.0381

ᵃ Removal under these conditions was attributed merely to the adsorption step.

© 2025 The Author(s). Published by the Royal Society of Chemistry

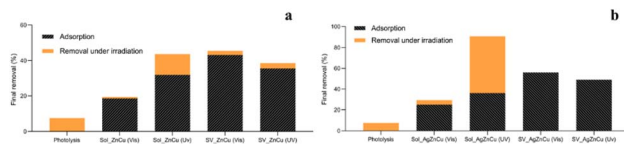Environ. Sci.: Adv., 2025, **4**, 1412–1426 | **1419**

Fig. 7 Photocatalytic degradation of MG over time using Zn0.5Cu0.5Fe$_2$O$_4$ synthesized by sol−gel and solvothermal methods, followed by silver doping: (a) non-functionalized; (b) Ag functionalized nanoparticles.

Fig. 8 Activity of Zn0.5Cu0.5Fe$_2$O$_4$ synthesized by sol−gel and functionalized with different amounts of silver: (a) adsorption assays with visible light irradiation assays with Sol_AgZnCu; (b) final removal.

with Sol_AgZnCu, with a 10-fold increase in the photodegradation rate (90.66%, 0.1589 h^{-1}) under UV irradiation when compared with Sol_ZnCu. Silver coupling can enhance the photoelectric properties of nanomaterials.[54] It acts as an electron trapper, improving charge separation efficiency and reducing recombination, which is typically observed in ferrite nanoparticles. The plasmonic effect of silver can also enhance catalytic performance through the generation of hot electrons. Specifically, under light excitation, the localized surface plasmon resonance of Ag nanoparticles produces energetic hot electrons, which may be transferred into the conduction band of the semiconductor. This process promotes more efficient charge separation and facilitates electron transfer to the catalyst surface, thereby contributing to improved photocatalytic activity. Under visible light, the removal rate was small, but it still was 3.7-fold higher than for particles without silver. Both results indicate that the presence of silver enhances the activity of the nanomaterials. This can be explained by the fact that the incorporation of Ag promotes the generation of reactive species by increasing the internal flow of electrons, thereby inhibiting recombination of charge carriers in photoexcited ferrite. This effect is particularly pronounced under UV irradiation.[55,56] On the contrary, the results with SV_AgZnCu sample demonstrated that on SV_ZnCu, silver does not exhibit the same improvements in photocatalytic activity. It appears that silver does not synergize as efficiently with the nanomaterials formed by the solvothermal method as with those synthesized by the sol–gel probably due to the presence of synthesis-related residues on the surface of the SV_ZnCu nanoparticles, which may hinder the effective interaction between silver and the catalyst, thereby reducing its performance. Overall, results elucidate that the nanomaterials synthesized by the sol–gel method presented substantially more solid results.

Adsorption was identified as a key process influencing the performance of the synthesized nanomaterials, with observable variations between batches of the same sample attributed to different levels of nanoparticle aggregation. To ensure the accuracy and reliability of comparisons, it is essential to use nanomaterials from a same batch. Of the two synthesis methods evaluated, the sol–gel method was chosen due to superior performance of nanomaterials synthesised by this method, which was further explored in the subsequent assays. Also, the silver reduction method was optimized (S2), as described in the previous section.

3.2.2. Effect of Ag coupling on Zn$_{0.5}$Cu$_{0.5}$Fe$_2$O$_4$ nanoparticles. Different ratios of NPs : Ag (1 : 1, 1 : 2, 1 : 3.5, 1 : 5, 1 : 10) were tested to address the optimal silver content (batch S2).
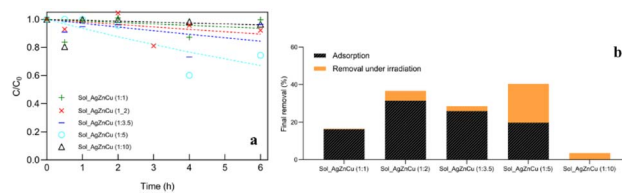
It is known that low silver percentages are insufficient to significantly enhance the photocatalytic process. Conversely, excessive silver amounts can obstruct the nanomaterial surface, thereby inhibiting the catalytic process by blocking ROS formation from the ferrite surface.[55] Indeed, the results showed that the optimal silver content ratio for the nanoparticles synthesised in this study was 1 : 5 (Table 2 and Fig. 8). In these 1 : 5 samples, the photocatalytic behaviour was notably enhanced under visible light with a rate constant of 0.0665 h^{-1} leading to an overall 40.39% MG removal.

Regarding the initial adsorption with various NPs : Ag ratios, the nanoparticles exhibited increased adsorption capacity up to a 1 : 2 ratio, likely due to enhanced dispersion of the nanoparticles facilitated by the presence of silver in the structure. However, as the amount of silver increased, exposure of the ferrite surface decreased, thereby suppressing the adsorption capacity of the cationic dye. At a 1 : 10 ratio, the adsorption capacity was entirely suppressed. A 1 : 5 doping ration was selected in the subsequent steps, as it demonstrated the best photocatalytic potential among the tested ratios.

3.2.3. Effect of photocatalyst concentration. The concentration of photocatalysts in the solution plays a critical role in the photocatalytic efficiency of a nanomaterial. If the photocatalyst concentration is too high, it can block light penetration into the solution, thereby hindering the photocatalytic process either by absorption at the first millimetres of the cuvette holding the sample or due to a "mirror effect" that occurs by reflecting or scattering light, reducing its interaction with the photocatalyst.[57,58]

Different concentrations of the nanomaterial Sol_AgZnCu (1 : 5) were tested under visible light to investigate the ideal concentration among the ones tested (Table 2 and Fig. 9). The lowest concentration assessed was 0.18 g L^{-1}, reaching a removal of almost 19.55% (at a rate of 0.0334 h^{-1}). Efficient light penetration enabled a good photon absorption by the
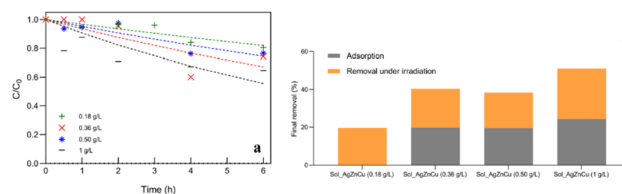

Fig. 9 Colour decreasing using different concentrations of Sol_AgZnCu (1 : 5): (a) activity under irradiation; (b) final removal considering both adsorption and degradation.

nanoparticles, with negligible adsorption (Table 3). Doubling photocatalyst concentration to 0.36 g L^{-1} resulted in a doubling of the photocatalytic rate (0.0665 h^{-1}) and of the final removal (40.39%). With this concentration, initial adsorption drastically increases due to a greater availability of active sites. As the concentration reached 0.5 g L^{-1}, the final removal obtained was similar to the obtained with 0.36 g L^{-1}, 38.32%, with a similar initial adsorption but at a 1.35-fold lower rate (0.0491 h^{-1}). This decrease in the rate constant may be due to a lower light penetration. The highest concentration tested, 1 g L^{-1}, caused the greater adsorption capacity, 24.26% (Table 3), but light penetration was considerably reduced. The final removal reached 51.08% (at a rate of 0.0982 h^{-1}), representing the best result in terms of MG removal, despite being mainly due to adsorption. Despite the overall improvement, the difference in photocatalytic efficiency between using 0.36 g L^{-1} and 1 g L^{-1} of catalyst was only 10%. Therefore, increasing the concentration to 1 g L^{-1} would raise process financial costs. Consequently, 0.36 g L^{-1} of Sol_AgZnCu (1 : 5) was considered the optimal concentration among those tested.

3.2.4. Extended UV and visible light irradiation time under optimal conditions. Extended UV and visible light irradiation time was tested for the best conditions given by the previous assays, i.e., 0.36 g L^{-1} of Sol_AgZnCu (1 : 5). A concentration of 0.75 g L^{-1} was also tested to determine if a higher nanomaterial concentration in prolonged visible light exposure and under UV would enhance the overall photodegradation. The results are presented in Table 2 and Fig. 10. With 0.36 g L^{-1}, under visible irradiation, increasing time from 6 h to 18 h did not cause significant differences in the final dye removal, and the rate was even lower (Table 3). This behaviour could be due to the suppression of active sites by the degradation products of the dye that remains adsorbed. Increasing the catalyst to 0.75 g L^{-1} increased the extent and the rate of dye removal: circa 62%, at a rate of 0.0381 h^{-1}. When comparing the results for 0.75 g L^{-1} with those for 1 g L^{-1} of catalyst, the decolorization rate was lower at the lowest catalyst concentration. Still, the overall degree of decolorization was slightly higher. This slightly lower concentration may enable more efficient light penetration.

Under UV irradiation, a final removal of 71.35% was achieved after 12 hours of irradiation (rate of 0.1033 h^{-1}), with a catalyst at a concentration of 0.36 g L^{-1}. Under the same concentration but using visible light, the final removal was 43.05% over 18 h (rate of 0.0218 h^{-1}). At a catalyst concentration of 0.75 g L^{-1}, the final removal under UV light was 58.52% (rate = 0.0730 h^{-1}), which is lower than the results obtained under

lower concentrations. Thus, increasing the concentration does not offer any additional advantage. Contrary, an increase in activity is observed under visible light, with the increase in catalyst concentration to 0.75 g L^{-1}, reaching 61.54% (at a rate of 0.052 h^{-1}).

In the first assays, using nanomaterials from batch S1, a 90% removal was achieved, a result not observed in the current assays. This discrepancy is attributed to the lower contribution of adsorption, which is likely due to a stronger binding of silver to the nanoparticle in the later batch (S2).

Recent studies on photocatalytic degradation of MG have reported various materials, such as MnFe$_2$O$_4$ and TiO$_2$ composites, showing promising activity under visible light when combined with additives like H$_2$O$_2$ to enhance oxidative species generation.[59] However, the present study introduces a silver-modified zinc-copper ferrite nanoparticle (AgZn$_{0.5}$-Cu$_{0.5}$Fe$_2$O$_4$) that shows effective MG degradation under exclusive visible light irradiation without the need for external oxidants. This offers both economic and operational advantages, especially in low-resource settings.

3.3. Mechanisms of MG photocatalytic removal

The photocatalytic assays revealed that adsorption significantly contributes to the removal process where the nanomaterials interact with MG molecules, binding them to the active sites. Upon irradiation, electron–hole (e$^-$/h$^+$) pairs are generated. However, due to their narrow bandgaps, ferrite nanomaterials present limiting charge separation, suppressing their efficiency. The coupling of silver at the surface of the catalysts, acting as an electron acceptor, promotes the internal electron charge flow, reducing the recombination tendency, thereby enhancing the photocatalytic activity and visible light absorption.[60] Silver nanoparticles, through their plasmonic properties, facilitate the transfer of hot electrons to the ZnCu ferrite surface, improving charge separation and prolonging the lifetime of the charge carriers. This enhances the generation of ROS, such as $^\bullet$OH and O$_2$$^{\bullet-}$, leading to more effective degradation of pollutants, compared to the un-coupled nanomaterial. Additionally, the
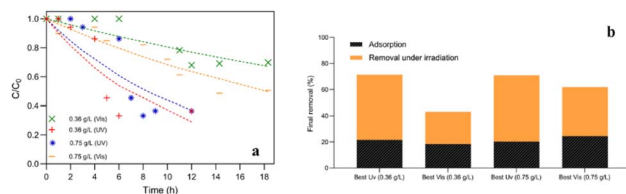

Fig. 10 Assays using the best conditions for different photocatalyst concentration of (a) 0.36 g L^{-1} and (b) 0.75 g L^{-1}; (c) final removal of the performed assays using the best conditions.
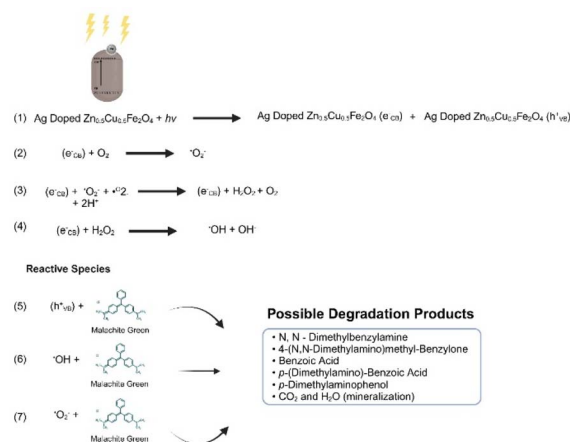

Fig. 11 Representation of the proposed mechanisms for the degradation of MG using Ag doped Zn$_{0.5}$Cu$_{0.5}$Fe$_2$O$_4$.

© 2025 The Author(s). Published by the Royal Society of Chemistry

Environ. Sci.: Adv., 2025, 4, 1412–1426 | 1421

formation of Ag-semiconductor heterojunctions improves interfacial charge transfer dynamics, further contributing to the separation of photoinduced charges. The increased visible light absorption, combined with improved electron mobility and reduced recombination rates, results in higher photocatalytic efficiency. These synergistic effects highlight the functional role of Ag in optimizing the photocatalytic mechanism and confirm its critical contribution to the superior performance of the $AgZn_{0.5}Cu_{0.5}Fe_2O_4$ nanomaterial.

A mechanism for the photocatalytic degradation of MG dye using Ag-doped $Zn_{0.5}Cu_{0.5}Fe_2O_4$ nanoparticles functionalized with silver is proposed based on the obtained results and supported by the works of Guandao et al.[61] and Zetra et al.[62] As illustrated in Fig. 11, the degradation of the dye is mainly driven by the action of photogenerated holes (h^+), superoxide anions ($^{\bullet}O_2^-$) and hydroxyl radicals ($^{\bullet}OH$). The photogenerated holes (h^+) can directly attack the dye molecules or react with OH^- or water molecules, forming $^{\bullet}OH$ radicals. However, according to the reduction potentials of $^{\bullet}OH/^-OH$ (1.99 eV) and $^{\bullet}OH/H_2O$ (2.31 eV) pairs, this reaction is unlikely to occur under these conditions. According to literature $Zn_{0.5}Cu_{0.5}Fe_2O_4$ conduction band edge is estimated to be between −1.10 eV for $ZnFe_2O_4$ and -0.92 eV for $CuFe_2O_4$, which renders this process ineffective.[63,64] The valence band edge is reported to be between 1.08 eV for $ZnFe_2O_4$ and 1.03 eV for $CuFe_2O_4$ (ref. 63 and 64). Excited electrons in the conduction band tend to form superoxide anions ($^{\bullet}O_2^-$) through reaction with the dissolved oxygen, which is favorable because the conduction band edge is more negative than the redox potential of $O_2/^{\bullet}O_2^-$ (0.33 eV).

Reactive species attacking the dye may generate various degradation products depending on the degradation pathways. For example, $^{\bullet}OH$ radicals can specifically target the central carbon atoms in MG structure, as described by Guandao et al.[61] This can lead to the formation of species like N,N-dimethylbenzylamine. Subsequent cleavage of the C–C bonds can produce 4-(N,N-dimethylamino)methylbenzylone. The photocatalytic reaction can further yield compounds such as benzoic acid, p-(dimethylamino)-benzoic acid and p-dimethylaminoethanol, ultimately leading to the formation of inert species like water and carbon dioxide, resulting in complete degradation.

3.4. Toxicity assessment

Toxicity assessment is crucial when evaluating the efficiency of photocatalytic pollutant removal efficiency, as degradation intermediates may persist in the treated effluent depending on the extent of pollutant degradation. This raises the need to evaluate whether the final effluent is more, equally or less toxic than the initial sample, ensuring that the treatment not only removes the original pollutant but also addresses any potential toxicity of the resulting compounds. To this end, the toxicity of the samples, both before and after the photocatalytic treatment, was assessed using the standard bioassay with V. fischeri as part of biosensor. V. fischeri is a highly sensitive bioluminescent microorganism that emits light from its metabolic activity.[65,66] The extent of luminescence inhibition, indicating toxicity, is shown in Table 4.

The initial MG solution at a concentration of 10 mg L⁻¹ caused a luminescent inhibition of 99.45%, indicating a level of toxicity considered "very toxic" towards Vibrio fischeri.[67,68] The initial MG solution at a concentration of 10 mg L⁻¹ caused a luminescent inhibition of 99.45%, indicating a level of toxicity considered "very toxic" towards Vibrio fischeri. Berberidou et al.,[69] similarly reported that a 10 mg L⁻¹ MG solution is extremely ecotoxic, completely inhibiting the bioluminescence

Table 4 Luminescence inhibition (%) of the samples before and after the photocatalytic treatment, towards *Vibrio fischeri*

	Sample	Nanomaterial concentration (g L⁻¹)	Light source	Time (h)	Luminescence inhibition (%)	Toxicity interpretation
Controls	MG (10 mg L⁻¹)	—	—	0	99.45 ± 0.12	Very toxic
	$AgZn_{0.5}Cu_{0.5}Fe_2O_4$	0.75	Visible	12	23.9 ± 7.7	Slightly toxic
Effect of photocatalyst concentrations	Sol_ZnCu	0.36	Visible	0	99.25 ± 0.08	Very toxic
	Sol_ZnCu	0.36	Visible	6	99.30 ± 0.40	Very toxic
	Sol_ZnCu	0.36	UV	0	99.72 ± 0.14	Very toxic
	Sol_ZnCu	0.36	UV	6	99.41 ± 0.33	Very toxic
	Sol_AgZnCu (1 : 5)	0.18	Visible	0	99.69 ± 0.13	Very toxic
	Sol_AgZnCu (1 : 5)	0.18	Visible	6	97.50 ± 0.23	Very toxic
	Sol_AgZnCu (1 : 5)	0.36	Visible	0	99.72 ± 0.04	Very toxic
	Sol_AgZnCu (1 : 5)	0.36	Visible	6	99.78 ± 0.10	Very toxic
	Sol_AgZnCu (1 : 5)	0.50	Visible	0	95.15 ± 4.22	Very toxic
	Sol_AgZnCu (1 : 5)	0.50	Visible	6	99.15 ± 0.82	Very toxic
	Sol_AgZnCu (1 : 5)	1.00	Visible	0	99.98 ± 0.00	Very toxic
	Sol_AgZnCu (1 : 5)	1.00	Visible	6	99.71 ± 0.21	Very toxic
Best conditions and prolonged irradiation	Sol_AgZnCu (1 : 5)	0.36	UV	0	99.73 ± 0.24	Very toxic
	Sol_AgZnCu (1 : 5)	0.36	UV	12	96.41 ± 1.31	Very toxic
	Sol_AgZnCu (1 : 5)	0.36	Visible	0	99.93 ± 0.03	Very toxic
	Sol_AgZnCu (1 : 5)	0.36	Visible	18.3	98.76 ± 0.76	Very toxic
	Sol_AgZnCu (1 : 5)	0.75	UV	0	99.88 ± 0.01	Very toxic
	Sol_AgZnCu (1 : 5)	0.75	UV	12	98.65 ± 1.50	Very toxic
	Sol_AgZnCu (1 : 5)	0.75	Visible	0	98.87 ± 0.48	Very toxic
	Sol_AgZnCu (1 : 5)	0.75	Visible	18.3	99.83 ± 0.12	Very toxic

1422 | *Environ. Sci.: Adv.*, 2025, **4**, 1412–1426

© 2025 The Author(s). Published by the Royal Society of Chemistry

of *V. fischeri*. Hernando *et al.*[68] reported an EC_{50} value of 0.031 mg L^{-1} for MG after 30 min of exposure to *V. fischeri*, highlighting its high toxicity. The toxic character of MG may be attributed to its lipophilic nature, which enables it to easily pass through the bacterial phospholipid bilayer. This same characteristic, in humans may potentially lead to carcinogenesis, mutagenesis, teratogenicity and respiratory toxicity.[70] After photocatalytic treatment, all the samples remained highly toxic, with luminescence inhibition values exceeding 98% (Table 4), despite the high MG removal percentage observed in the photocatalytic assays (Fig. 9 and 10). This could be explained by the toxicity of the dye, which persists even at low concentrations in the treated solution (0.93 mg L^{-1}), but also by the potentially more toxic degradation by-products formed during the degradation process. This is consistent with previous published works observing the formation of degradation by-products from the photocatalytic degradation of pollutants, that are more toxic than the parent compound.[70,71] For instance, Pérez-Estrada *et al.*[71] conducted the photolytic degradation of MG, resulting in a large number of degradation by-products that were more persistent and toxic than the parent compound. They identified 28 possible by-products, with the molecule 4-(dimethylamino) benzophenone ($C_{15}H_{16}NO$) being detected at the highest concentration after 220 h of exposure to natural sunlight. After photocatalytic treatment, the concentration of this compound was still over its EC_{50} value towards *V. fischeri* (EC_{50} of 0.061 mg L^{-1}), indicating that it strongly contributed to the toxicity of the treated effluent.[71] Therefore, extending the irradiation assays to promote complete mineralization of the compounds is crucial to reduce the toxicity of the treated sample.

4. Conclusions

The photocatalytic degradation efficiency of Ag-doped $Zn_{0.5}$-$Cu_{0.5}Fe_2O_4$ nanoparticles functionalized *via* a reduction method was successfully evaluated. $Zn_{0.5}Cu_{0.5}Fe_2O_4$ demonstrated good photocatalytic potential, attributed to its stability and narrow bandgap. Two synthesis methods, sol–gel and solvothermal, were compared for producing $Zn_{0.5}Cu_{0.5}Fe_2O_4$, with the sol–gel method demonstrating superior performance in terms of photocatalytic activity. Despite the inherent challenge of high electrons/holes recombination in the ferrite nanomaterials, silver doping significantly enhanced their photocatalytic performance. The silver reduction process notably increased the photocatalytic activity of the nanoparticles, rendering them active under visible light. The photocatalytic activity of the nanoparticles under visible light offers significant potential for utilizing natural sunlight or low-energy artificial light sources with visible wavelengths. An important aspect of this catalytic process is that it does not require the addition of external agents, such as H_2O_2. Our approach isolates the irradiation component, using only visible light, as opposed to solar light which also includes UV radiation. This adds another layer of simplicity and efficiency to the photocatalytic process, making it more straightforward for practical applications where only visible light is available. Moreover, the nanoparticles demonstrated a high adsorption capacity, which is a critical factor for efficient dye removal and subsequent photocatalytic degradation. This capability enables the removal of cationic dyes, such as MG, even in the absence of light. Notably, a considerable proportion of the dye can be removed within just one hour without any light exposure. This characteristic is particularly advantageous for applications involving contaminated waters with lower dye concentrations and limited light availability. Additionally, the superparamagnetic properties of the nanoparticles facilitate their easy removal from the reaction medium. This study concludes that $Zn_{0.5}Cu_{0.5}Fe_2O_4$ nanoparticles, synthesized *via* the sol–gel method and coupled with silver, are active under visible light and efficient in removing pollutants such as dyes, under both UV and visible light irradiation.

The study identified several key areas for further development that will help elevate the process to a higher level of efficiency and applicability. An optimized cleaning process is essential to enhance the photocatalytic activity of SV_AgZnCu and render the nanomaterials suitable for potential industrial applications. The Sol_AgZnCu nanomaterial is well-suited for degrading low residual concentrations of dye, though it exhibits some saturation due to the accumulation of adsorbed degradation products. This makes it effective in the final stages of wastewater treatment, where the organic load is lower and micropollutants are targeted. Refining the silver reduction methodology could further boost photocatalytic activity, reduce dye toxicity, and shorten the required irradiation time. Addressing these aspects will enhance both the efficiency and industrial relevance of the developed nanomaterials.

Data availability

Data supporting this article is available at **https://drive.google.com/drive/folders/1o1GzTTMzdpqW5nqdFvei8 3iiDgqIgTIv?usp=drive_link**.

Author contributions

Conceptualization, Ricardo J. C. Fernandes, Luciana Pereira and Paulo J. G. Coutinho; methodology, Ricardo J. C. Fernandes, Beatriz D. Cardoso, Ana Rita Silva, Luciana Pereira and Paulo J. G. Coutinho; supervision, Luciana Pereira and Paulo J. G. Coutinho; writing-original draft, Ricardo J. C. Fernandes; writing-review and editing, Luciana Pereira and Paulo J. G. Coutinho. All authors have read and agreed to the published version of the manuscript.

Conflicts of interest

There are no conflicts to declare.

Notes and references

1 R. Noor, *et al.*, A comprehensive review on water pollution, South Asia Region: Pakistan, *Urban Clim.*, 2023, **48**, 101413, DOI: **10.1016/j.uclim.2023.101413**.

© 2025 The Author(s). Published by the Royal Society of Chemistry

Environ. Sci.: Adv., 2025, **4**, 1412–1426 | **1423**

2 E. K. Nti, *et al.*, Water pollution control and revitalization using advanced technologies: Uncovering artificial intelligence options towards environmental health protection, sustainability and water security, *Heliyon*, 2023, **9**(7), e18170, DOI: **10.1016/j.heliyon.2023.e18170**.

3 M. M. M. Syeed, M. S. Hossain, M. R. Karim, M. F. Uddin, M. Hasan and R. H. Khan, Surface water quality profiling using the water quality index, pollution index and statistical methods: A critical review, *Environ. Sustain. Indic.*, 2023, **18**, 100247, DOI: **10.1016/j.indic.2023.100247**.

4 V. Balaram, L. Copia, U. S. Kumar, J. Miller and S. Chidambaram, Pollution of water resources and application of ICP-MS techniques for monitoring and management—A comprehensive review, *Geosystems Geoenvironment*, 2023, **2**(4), 100210, DOI: **10.1016/j.geogeo.2023.100210**.

5 J. Xue, Q. Wang and M. Zhang, A review of non-point source water pollution modeling for the urban–rural transitional areas of China: Research status and prospect, *Sci. Total Environ.*, 2022, **826**, 154146, DOI: **10.1016/j.scitotenv.2022.154146**.

6 N. H. H. Hairom, *et al.*, A review of nanotechnological applications to detect and control surface water pollution, *Environ. Technol. Innov.*, 2021, **24**, 102032, DOI: **10.1016/j.eti.2021.102032**.

7 Y. Song, L. Wang, X. Qiang, W. Gu, Z. Ma and G. Wang, An overview of biological mechanisms and strategies for treating wastewater from printing and dyeing processes, *J. Water Process Eng.*, 2023, **55**, 104242, DOI: **10.1016/j.jwpe.2023.104242**.

8 F. Karimi, *et al.*, Natural waste-derived nano photocatalysts for azo dye degradation, *Environ. Res.*, 2023, **238**, 117202, DOI: **10.1016/j.envres.2023.117202**.

9 R. Al-Tohamy, *et al.*, A critical review on the treatment of dye-containing wastewater: ecotoxicological and health concerns of textile dyes and possible remediation approaches for environmental safety, *Ecotoxicol. Environ. Saf.*, 2022, **231**, 113160, DOI: **10.1016/j.ecoenv.2021.113160**.

10 C. Keshava, *et al.*, Application of systematic evidence mapping to identify available data on the potential human health hazards of selected market-relevant azo dyes, *Environ. Int.*, 2023, **176**, 107952, DOI: **10.1016/j.envint.2023.107952**.

11 S. Nassar, A. E. D. H. Sayed, N. Allam Nafady, M. M. Ali and E. M. Mohamed, Bioremediation of the toxic effects induced by the malachite green dye in *Clarias gariepinus* using *Rhodotorula mucilaginosa* MH298827, *Sci. African*, 2024, **26**, e02496, DOI: **10.1016/j.sciaf.2024.e02496**.

12 J. Sharma, S. Sharma and V. Soni, Toxicity of malachite green on plants and its phytoremediation: a review, *Reg. Stud. Mar. Sci.*, 2023, **62**, 102911, DOI: **10.1016/j.rsma.2023.102911**.

13 E. Panel and F. Chain, Malachite green in food, *EFSA J.*, 2016, **14**(7), 4530, DOI: **10.2903/j.efsa.2016.4530**.

14 H. N. Ahamed, *et al.*, Investigating the toxicity of malachite green and copper sulfate in brine shrimp: *in vivo* and computational study, *Toxicol. Reports*, 2024, **13**, 101811, DOI: **10.1016/j.toxrep.2024.101811**.

15 A. V. Mohod, *et al.*, Degradation of Rhodamine dyes by Advanced Oxidation Processes (AOPs) – focus on cavitation and photocatalysis – a critical review, *Water Resour. Ind.*, 2023, **30**, 100220, DOI: **10.1016/j.wri.2023.100220**.

16 S. Bibi, *et al.*, Cu-doped mesoporous TiO_2 photocatalyst for efficient degradation of organic dye *via* visible light photocatalysis, *Chemosphere*, 2023, **339**, 139583, DOI: **10.1016/j.chemosphere.2023.139583**.

17 U. Sirisha, B. Sowjanya, H. Rehana Anjum, T. Punugoti, A. Mohamed and M. Vangalapati, Synthesized TiO_2 nanoparticles for the application of photocatalytic degradation of synthetic toxic dye acridine orange, *Mater. Today Proc.*, 2022, **62**, 3444–3449, DOI: **10.1016/j.matpr.2022.04.278**.

18 F. Du, *et al.*, SiO_2/Ga_2O_3 nanocomposite for highly efficient selective removal of cationic organic pollutant *via* synergistic electrostatic adsorption and photocatalysis, *Sep. Purif. Technol.*, 2022, **295**, 121221, DOI: **10.1016/j.seppur.2022.121221**.

19 K. K. Pawar, *et al.*, In_2O_3 nanocapsules for rapid photodegradation of crystal violet dye under sunlight, *J. Colloid Interface Sci.*, 2020, **561**, 287–297, DOI: **10.1016/j.jcis.2019.10.101**.

20 M. Wang, X. Wang, M. Wang and J. Han, Mesoporous In_2O_3 nanorods/In_2S_3 nanosheets hierarchical heterojunctions toward highly efficient visible light photocatalysis, *J. Alloys Compd.*, 2022, **921**, 165973, DOI: **10.1016/j.jallcom.2022.165973**.

21 N. Arumugham, A. Mariappan, J. Eswaran, S. Daniel, R. Kanthapazham and P. Kathirvel, Nickel ferrite-based composites and its photocatalytic application – a review, *J. Hazard. Mater. Adv.*, 2022, **8**(July), 100156, DOI: **10.1016/j.hazadv.2022.100156**.

22 T. Ajeesha, *et al.*, Nickel substituted $MgFe_2O_4$ nanoparticles *via* co-precipitation method for photocatalytic applications, *Phys. Rev. B:Condens. Matter Mater. Phys.*, 2021, **606**, 412660, DOI: **10.1016/j.physb.2020.412660**.

23 V. Lakshmi Ranganatha, S. Pramila, G. Nagaraju, H. N. Udayabhanu, B. S. Surendra and C. Mallikarjunaswamy, Cost-effective and green approach for the synthesis of zinc ferrite nanoparticles using *Aegle marmelos* extract as a fuel: catalytic, electrochemical, and microbial applications, *J. Mater. Sci. Mater. Electron.*, 2020, **31**(20), 17386–17403, DOI: **10.1007/s10854-020-04295-6**.

24 A. V. Bagade, S. N. Pund, P. A. Nagwade, B. Kumar, S. U. Deshmukh and A. B. Kanagare, Ni-doped Mg-Zn nano-ferrites: fabrication, characterization, and visible-light-driven photocatalytic degradation of model textile dyes, *Catal. Commun.*, 2023, **181**, 106719, DOI: **10.1016/j.catcom.2023.106719**.

25 N. S. Al-Bassami, S. F. Mansour, E. Abdel-Fattah and M. A. Abdo, Ce-Co-Mn-Zn ferrite nano catalyst: a synergetic effect of rare earth Ce^{3+} on enhanced optical properties and photocatalysis, *Ceram. Int.*, 2023, **49**(12), 20601–20612, DOI: **10.1016/j.ceramint.2023.03.191**.

26 N. Aladdin Jasim, S. Esmail Ebrahim and S. H. Ammar, Fabrication of $Zn_xMn_{1-x}Fe_2O_4$ metal ferrites for boosted

photocatalytic degradation of rhodamine-B dye, *Results Opt.*, 2023, **13**(June), 100508, DOI: **10.1016/j.rio.2023.100508**.

27 A. H. Alshammari, *et al.*, Low temperature sol-gel synthesis of copper zinc ferrite for hydrogen catalytic hydrolysis of sodium borohydride, *Mater. Chem. Phys.*, 2023, **308**, 128287, DOI: **10.1016/j.matchemphys.2023.128287**.

28 S. Sasikumar and A. Rajaram, The synergetic effect of cobalt-doped zinc ferrite and hexagonal boron nitride photocatalyst for wastewater treatment, *Diam. Relat. Mater.*, 2024, **147**, 111270, DOI: **10.1016/j.diamond.2024.111270**.

29 A. Tony Dhiwahar, M. Sundararajan, P. Sakthivel, C. S. Dash and S. Yuvaraj, Microwave-assisted combustion synthesis of pure and zinc-doped copper ferrite nanoparticles: structural, morphological, optical, vibrational, and magnetic behavior, *J. Phys. Chem. Solids*, 2020, **138**, 109257, DOI: **10.1016/j.jpcs.2019.109257**.

30 F. Ahmad Abuilaiwi, M. Awais, U. Y. Qazi, F. Ali and A. Afzal, Al^{3+} doping reduces the electron/hole recombination in photoluminescent copper ferrite ($CuFe_{2-x}Al_xO_4$) nanocrystallites, *Bol. Soc. Espanola Ceram. Vidr.*, 2022, **61**(3), 252–262, DOI: **10.1016/j.bsecv.2020.11.007**.

31 R. J. C. Fernandes, *et al.*, Photodeposition of silver on zinc/calcium ferrite nanoparticles: a contribution to efficient effluent remediation and catalyst reutilization, *Nanomaterials*, 2021, **11**(4), 1–13, DOI: **10.3390/nano11040831**.

32 R. J. C. Fernandes, *et al.*, Zinc/Magnesium Ferrite Nanoparticles Functionalized with Silver for Optimized Photocatalytic Removal of Malachite Green, *Materials*, 2024, **17**(13), 3158, DOI: **10.3390/ma17133158**.

33 M. Tsvetkov, J. Zaharieva and M. Milanova, Ferrites, modified with silver nanoparticles, for photocatalytic degradation of malachite green in aqueous solutions, *Catal. Today*, 2020, **357**, 453–459, DOI: **10.1016/j.cattod.2019.07.052**.

34 G. Palanisamy, K. Bhuvaneswari, A. Chinnadurai, G. Bharathi and T. Pazhanivel, Magnetically recoverable multifunctional $ZnS/Ag/CoFe_2O_4$ nanocomposite for sunlight driven photocatalytic dye degradation and bactericidal application, *J. Phys. Chem. Solids*, 2020, **138**, 109231, DOI: **10.1016/j.jpcs.2019.109231**.

35 X. Zhang, L. Shi and Y. Zhang, Preparation of organic–inorganic PDI/BiO_{2-x} photocatalyst with boosted photocatalytic performance, *J. Taiwan Inst. Chem. Eng.*, 2022, **132**, 104111, DOI: **10.1016/j.jtice.2021.10.011**.

36 N. Pugazhenthiran, *et al.*, Silver nanoparticles modified ZnO nanocatalysts for effective degradation of ceftiofur sodium under UV-vis light illumination, *Chemosphere*, 2023, **313**, 137515, DOI: **10.1016/j.chemosphere.2022.137515**.

37 L. Fan, *et al.*, Relationship between photolysis mechanism and photo-enhanced toxicity to *Vibrio fischeri* for neonicotinoids with cyano-amidine and nitroguanidine structures, *Aquat. Toxicol.*, 2023, **257**, 106443, DOI: **10.1016/j.aquatox.2023.106443**.

38 I. Milenković, *et al.*, Toxicity investigation of CeO_2 nanoparticles coated with glucose and exopolysaccharides levan and pullulan on the bacterium *Vibrio fischeri* and aquatic organisms *Daphnia magna* and *Danio rerio*, *Aquat. Toxicol.*, 2021, **236**, 105867, DOI: **10.1016/j.aquatox.2021.105867**.

39 A. R. Silva, *et al.*, Ciprofloxacin wastewater treated by UVA photocatalysis: contribution of irradiated TiO_2 and ZnO nanoparticles on the final toxicity as assessed by *Vibrio fischeri*, *RSC Adv.*, 2016, **6**(98), 95494–95503, DOI: **10.1039/c6ra19202e**.

40 I. Standard and T. Standard, *ISO 11348-1*, vol. 1998, 1998.

41 W. E. F., Standard Methods Committee of the American Public Health Association, American Water Works Association, "ISO 114348-3 – Water quality-Determination of the inhibitory effect of water samples on te light emission of vibrio fischeri (Luminescent bacteria test)- Part 3: Method using freeze-dried bacteria," *Stand. Methods Exam. Water Wastewater*, 2023, **2007**, 1–21.

42 A. R. Silva, *et al.*, Ph-induced modulation of *Vibrio fischeri* population life cycle, *Chemosensors*, 2021, **9**(10), 1–14, DOI: **10.3390/chemosensors9100283**.

43 A. R. Silva, M. S. Duarte, M. M. Alves and L. Pereira, Bioremediation of Perfluoroalkyl Substances (PFAS) by Anaerobic Digestion: Effect of PFAS on Different Trophic Groups and Methane Production Accelerated by Carbon Materials, *Molecules*, 2022, **27**(6), 1895, DOI: **10.3390/molecules27061895**.

44 N. Doebelin and R. Kleeberg, Profex: a graphical user interface for the Rietveld refinement program BGMN, *J. Appl. Crystallogr.*, 2015, **48**, 1573–1580, DOI: **10.1107/S1600576715014685**.

45 B. Kariuki and D. Cox, *Extended Software/Methods Development Issue*, no. 20, 1998.

46 E. Solano, *et al.*, Erratum: neutron and X-ray diffraction study of ferrite nanocrystals obtained by microwave-assisted growth. A structural comparison with the thermal synthetic route, *J. Appl. Crystallogr.*, 2014, **47**, 414–420, DOI: **10.1107/S1600576714017452**.

47 S. Sugi, S. Radhika and C. M. Padma, Photocatalytic and antibacterial activity of PVA mediated zinc-copper ferrite composites, *Mater. Today Proc.*, 2022, **64**, 1738–1744, DOI: **10.1016/j.matpr.2022.05.536**.

48 R. J. C. Fernandes, *et al.*, Magnetic nanoparticles of zinc/calcium ferrite decorated with silver for photodegradation of dyes, *Materials*, 2019, **12**(21), 3582, DOI: **10.3390/ma12213582**.

49 D. Nadhiya, *et al.*, Influence of Cu^{2+} substitution on the structural, optical, magnetic, and antibacterial behaviour of zinc ferrite nanoparticles, *J. Saudi Chem. Soc.*, 2023, **27**(5), 101696, DOI: **10.1016/j.jscs.2023.101696**.

50 M. A. Camacho-González, M. Quezada-Cruz, G. I. Cerón-Montes, M. F. Ramírez-Ayala, L. E. Hernández-Cruz and A. Garrido-Hernández, Synthesis and characterization of magnetic zinc-copper ferrites: Antibacterial activity, photodegradation study and heavy metals removal evaluation, *Mater. Chem. Phys.*, 2019, **236**, 121808, DOI: **10.1016/j.matchemphys.2019.121808**.

51 D. S. Mathew and R. S. Juang, An overview of the structure and magnetism of spinel ferrite nanoparticles and their

© 2025 The Author(s). Published by the Royal Society of Chemistry

Environ. Sci.: Adv., 2025, **4**, 1412–1426 | **1425**

synthesis in microemulsions, *Chem. Eng. J.*, 2007, **129**(1–3), 51–65, DOI: 10.1016/j.cej.2006.11.001.

52 N. Kaur and S. D. Tiwari, Superparamagnetic behavior of non-interacting antiferromagnetic ferritin nanoparticles, *J. Phys. Chem. Solids*, 2024, **185**, 111746, DOI: 10.1016/j.jpcs.2023.111746.

53 R. Guz, E. R. L. Tiburtius and C. A. Pessôa, Association of adsorption and heterogeneous photocatalysis in the degradation of tartrazine yellow dye with $CuNb_2O_6$ synthesized and immobilized on chitosan membranes, *Inorg. Chem. Commun.*, 2023, **152**, 110645, DOI: 10.1016/j.inoche.2023.110645.

54 S. Elbasuney, A. M. El-Khawaga, M. A. Elsayed and M. A. Correa-Duarte, Silver doped anatase nanocomposite: a novel photocatalyst with advanced activity under visible light for waste-water treatment, *Discov. Appl. Sci.*, 2024, **6**(4), 159, DOI: 10.1007/s42452-024-05804-6.

55 A. Bhava, U. S. Shenoy and D. K. Bhat, Silver doped barium titanate nanoparticles for enhanced visible light photocatalytic degradation of dyes, *Environ. Pollut.*, 2024, **344**(2023), 123430, DOI: 10.1016/j.envpol.2024.123430.

56 V. Madhavi, P. Kondaiah and G. Mohan Rao, Influence of silver nanoparticles on titanium oxide and nitrogen doped titanium oxide thin films for sun light photocatalysis, *Appl. Surf. Sci.*, 2018, **436**, 708–719, DOI: 10.1016/j.apsusc.2017.11.279.

57 C. Song, P. Chen, C. Wang and L. Zhu, Photodegradation of perfluorooctanoic acid by synthesized TiO_2-MWCNT composites under 365 nm UV irradiation, *Chemosphere*, 2012, **86**(8), 853–859, DOI: 10.1016/j.chemosphere.2011.11.034.

58 S. Sohrabnezhad, A. Pourahmad and E. Radaee, Photocatalytic degradation of basic blue 9 by CoS nanoparticles supported on AlMCM-41 material as a catalyst, *J. Hazard. Mater.*, 2009, **170**(1), 184–190, DOI: 10.1016/j.jhazmat.2009.04.108.

59 F. V. de Andrade, *et al.*, $MnFe_2O_4$ nanoparticulate obtained by microwave-assisted combustion: an efficient magnetic catalyst for degradation of malachite green cationic dye in aqueous medium, *J. Environ. Chem. Eng.*, 2021, **9**(5), 106232, DOI: 10.1016/j.jece.2021.106232.

60 E. A. Okba, F. E. Fakhry, H. H. El-Bahnasawy, M. M. Abdel-Galeil and R. E. El Shater, Development of heterogeneous photocatalysis delafossite structured Ag doped Cd-Cu ferrite spinel nanoparticles for an efficient photodegradation process, *J. Photochem. Photobiol., A*, 2024, **448**, 115275, DOI: 10.1016/j.jphotochem.2023.115275.

61 G. Gao, A. Zhang, M. Zhang, J. Chen and Q. Zhang, Photocatalytic Degradation Mechanism of Malachite Green under Visible Light Irradiation over Novel Biomimetic Photocatalyst HMS-FePcs, *Chinese J. Catal.*, 2008, **29**(5), 426–430, DOI: 10.1016/S1872-2067(08)60043-1.

62 Y. Zetra, *Photocatalytic degradation of malachite green using TiO₂ and O₂/UV Photocatalytic Degradation of Malachite Green using TiO₂*, vol. 020092, no. December 2018, 2020.

63 H. Song, L. Zhu, Y. Li, Z. Lou, M. Xiao and Z. Ye, Preparation of $ZnFe_2O_4$ nanostructures and highly efficient visible-light-driven hydrogen generation with the assistance of nanoheterostructures, *J. Mater. Chem. A*, 2015, **3**(16), 8353–8360, DOI: 10.1039/c5ta00737b.

64 S. Park, *et al.*, Rapid Flame-Annealed $CuFe_2O_4$ as Efficient Photocathode for Photoelectrochemical Hydrogen Production, *ACS Sustain. Chem. Eng.*, 2019, **7**(6), 5867–5874, DOI: 10.1021/acssuschemeng.8b05824.

65 E. Mendonc, *et al.*, Ecotoxicity tests in the environmental analysis of wastewater treatment plants: case study in Portugal, *J. Hazard. Mater.*, 2009, **163**, 665–670, DOI: 10.1016/j.jhazmat.2008.07.012.

66 A. R. Silva, O. S. G. P. Soares, M. F. R. Pereira, M. Madalena Alves and L. Pereira, Tailoring carbon nanotubes to enhance their efficiency as electron shuttle on the biological removal of acid orange 10 under anaerobic conditions, *Nanomaterials*, 2020, **10**(12), 1–19, DOI: 10.3390/nano10122496.

67 S. Gupta, L. G. Raikar, S. Kokate, J. Gandhi and H. Prakash, Evaluation of activated persulfate under real solar light for degradation of organic pollutants: kinetics, mechanism, and ecotoxicity, *J. Environ. Chem. Eng.*, 2023, **11**(5), 110313, DOI: 10.1016/j.jece.2023.110313.

68 M. D. Hernando, S. De Vettori, M. J. Martínez Bueno and A. R. Fernández-Alba, Toxicity evaluation with *Vibrio fischeri* test of organic chemicals used in aquaculture, *Chemosphere*, 2007, **68**(4), 724–730, DOI: 10.1016/j.chemosphere.2006.12.097.

69 C. Berberidou, I. Poulios, N. P. Xekoukoulotakis and D. Mantzavinos, Sonolytic, photocatalytic and sonophotocatalytic degradation of malachite green in aqueous solutions, *Appl. Catal., B*, 2007, **74**(1–2), 63–72, DOI: 10.1016/j.apcatb.2007.01.013.

70 S. Kokilavani, *et al.*, Efficient photocatalytic degradation of methyl orange and malachite green by Ag_3PO_4 decorated BiOBr nanoflower under visible light: performance evaluation, mechanism insights and toxicology of the by-products, *J. Alloys Compd.*, 2022, **909**, 164703, DOI: 10.1016/j.jallcom.2022.164703.

71 L. A. Pérez-Estrada, A. Agüera, M. D. Hernando, S. Malato and A. R. Fernández-Alba, Photodegradation of malachite green under natural sunlight irradiation: kinetic and toxicity of the transformation products, *Chemosphere*, 2008, **70**(11), 2068–2075, DOI: 10.1016/j.chemosphere.2007.09.008.

Environmental
Science
Advances

Light

Photocatalysts

e⁻

ROS

By-products

**ROYAL SOCIETY
OF CHEMISTRY**

PAPER
Luciana Pereira *et al.*
Potential of magnetic silver-coupled zinc and copper ferrite
nanoparticles as visible-light photocatalysts towards the
degradation of dyes